Effect of spin-orbit interaction on the vortex dynamics in LaAlO₃/SrTiO₃ interfaces near the superconducting transition

Gopi Nath Daptary [1,*] Hemanta Kumar Kundu,[1] Pramod Kumar,[2,†] Anjana Dogra,[2] Narayan Mohanta,[3] A. Taraphder,[4] and Aveek Bid[1,‡]

[1]*Department of Physics, Indian Institute of Science, Bangalore 560012, India*
[2]*National Physical Laboratory, New Delhi 110012, India*
[3]*Material Science and Technology Division, Oak Ridge National Laboratory, Oak Ridge, Tennessee 37831, USA*
[4]*Department of Physics and Centre for Theoretical Studies, Indian Institute of Technology Kharagpur, West Bengal 721302, India*

Controlling spin-orbit interaction and its effect on superconductivity has been a long-standing problem in two-dimensional inversion-symmetry-broken superconductors. An open challenge is to understand the role of various energy scales in shaping the complex phase diagram in these systems. From a combined experimental and theoretical study of resistance fluctuations and its higher-order statistics, we propose a phase diagram for the superconducting phase in the magnetic-field–spin-orbit interaction energy plane for the quasi-two-dimensional electron gas at the interface of LaAlO₃/SrTiO₃ heterostructures. The relative variance of resistance fluctuations increases by few orders of magnitude below the spin-orbit field B_{SO} and a non-Gaussian component to the fluctuations arises for fields below the upper critical field B_{c2}. Theoretical calculations show that the non-Gaussian noise predominantly arises due to percolative nature of the superconducting transition. We quantify the strength and the relative importance of the spin-orbit interaction energy, Zeeman energy, and the pairing potential. Our work highlights the important role played by the interplay between these energy scales in framing the fascinating phases seen in two-dimensional inversion-symmetry-broken superconductors.

I. INTRODUCTION

Unconventional superconductivity is of great interest both from theoretical as well as experimental points of view [1,2]. Anderson's theorem [3] states that in the presence of both time-reversal and inversion symmetries one gets even-parity spin-singlet pairing in superconductors. The absence of either one of these symmetries, either through Zeeman effect (loss of time-reversal symmetry) or spin-orbit interaction (loss of inversion symmetry) leads to the lifting of spin degeneracy favoring the formation of odd-parity spin-triplet Cooper pairs [4]. The effect of broken time-reversal symmetry on parity of Cooper pairs is pretty well studied. There are several examples of superconductors in nature where the presence of magnetism leads to the appearance of nontrivial pairing, well-known examples being heavy-fermion systems (e.g., CeIn₃ [5], CeCoIn₅ [6], and UGe₂ [7]), iron-pnictides [8], certain organic superconductors. On the other hand, known examples of naturally occurring odd-parity pairing induced by spin-orbit interaction (SOI) are much rarer, the obvious exceptions being noncentrosymmetric superconductors like CePt₃Si [9], CeIrSi₃ [10], and CeRhSi₃ [10,11]. Under certain conditions, odd-parity pairing can be induced in two-dimensional super-conductors in the presence of SOI [12,13].

The quasi-two-dimensional electron gas (q-2DEG) formed at the interface between (001)-oriented SrTiO₃ and LaAlO₃ (hereafter referred as LaAlO₃/SrTiO₃) is one such system. Two factors lead to the appearance of a large Rashba SOI in this system: (a) breaking of parity symmetry at the interface, and (b) a large electric field perpendicular to the interface, primarily due to polar catastrophe (and to a lesser extent due to applied back-gate voltage). It is interesting to note that Rashba SOI has two notable consequences: (a) it induces charge inhomogeneity at the interface at submicron length scales [14], and (b) it induces an in-plane field perpendicular to the k vector of the charge carriers [15]. Both these factors are expected to have a significant influence on superconductivity. Another advantage of this q-2DEG over conventional noncentrosymmetric bulk superconductors is that both superconducting T_C and SOI strength are gate-voltage tunable [16–18]. A variety of exotic phenomena have been theoretically predicted to exist as a consequence of the SOI including Fulde-Ferrell-Larkin-Ovchinikov–type (FFLO) superconductivity coexisting with ferromagnetism [13], exotic superconducting pairing states which are an admixture of spin-singlet and spin-triplet components [19,20] and emergent Majorana quasiparticles [21].

In this paper we present detailed experimental studies of the effect of SOI on the magnetotransport and spin fluctuations in high-quality LaAlO₃/SrTiO₃ heterostructures at temperatures much below the superconducting T_C. Study of second- as well as higher-order moments of fluctuations of dynamical variables is a well-established tool to probe the presence of long-range correlations in systems undergoing phase transitions [22–28]. From magnetotransport

---

*Current address: Department of Physics, Bar Ilan University, Ramat Gan 5290002, Israel.

†Current address: Department of Physics, St. John's College, Agra, Uttar Pradesh 282 002, India.

‡aveek@iisc.ac.in

measurements we identify the relevant field scales: upper critical field B_{c2} and spin-orbit field B_{SO}, which are gate voltage tunable. We observe that close to these field scales, resistance fluctuations and their higher-order statistics develop strikingly nontrivial features. Both from experimental and theoretical data, we find that the interplay between spin-orbit interaction, pairing energy, and Zeeman energy creates a fascinating phase diagram very distinct from that usually found for conventional two-dimensional (2D) superconductors.

II. EXPERIMENTAL DETAILS

Our measurements were performed on samples with 10 unit cells of LaAlO$_3$ grown by pulsed laser deposition (PLD) on TiO$_2$-terminated (001) SrTiO$_3$ single-crystal substrates. As received SrTiO$_3$ substrates were pretreated with standard buffered hydrofluoric (NH$_4$F - HF) solution [29] in order to achieve uniform TiO$_2$ termination. The TiO$_2$ termination of the substrate realized with the buffer HF solution etching was confirmed from atomic force microscopy measurements. Prior to deposition the treated substrates were annealed for an hour at $830\,°C$ in oxygen partial pressure of 7.4×10^{-2} mbar. The purpose of preannealing of substrates in oxygen atmosphere at $830\,°C$ was to remove any moisture and organic contaminants from the surface and also to reconstruct the surface so that pure TiO$_2$ termination is realized. Further, 10 unit cells of LaAlO$_3$ were deposited at $800\,°C$ at an oxygen partial pressure of 1×10^{-4} mbar. Growth with the precision of a single unit cell was monitored by the oscillations count using *in situ* reflection high-energy electron diffraction (RHEED) gun. The epitaxial nature of the films was confirmed by high-resolution x-ray diffraction (HRXRD) performed on a 20-unit-cell LaAlO$_3$ film grown under identical conditions on TiO$_2$-terminated SrTiO$_3$ which allowed us to measure the c-axis lattice parameter of LaAlO$_3$. The thickness of one unit cell from these measurements came out to be 3.75 Å [30]. Ohmic electrical contacts were achieved by ultrasonically bonding Au wires (25 μm diameter) at the four corners of the device in a van der Pauw geometry. This technique is known to breakdown the 10 unit cells of LaAlO$_3$ and provide Ohmic contact with the underlying electron gas [16,18,27,28,31–33]. All electrical measurements were performed in a cryogen-free dilution refrigerator over the temperature range 20–250 mK and magnetic field range 0–16 T. The relative angle between the magnetic field B and the q-2DEG could be changed by rotating the sample *in situ* the dilution refrigerator and measurements were done with B applied both parallel ($B_\parallel$) and perpendicular ($B_\perp$) to the interface. The charge carrier density at the interface was controlled using a back-gate voltage V_g with the SrTiO$_3$ acting as the dielectric material. Measurements were performed over the range -200 V $< V_g < 200$ V. The interface was found to be superconducting for all values of $V_g > -10$ V.

III. RESULTS AND DISCUSSION

We start with the results of magnetoresistance measurements at $V_g = 200$ V. The superconducting transition temperature T_C (defined as the temperature where the zero-field resistance became 40% of its normal-state value) was mea-
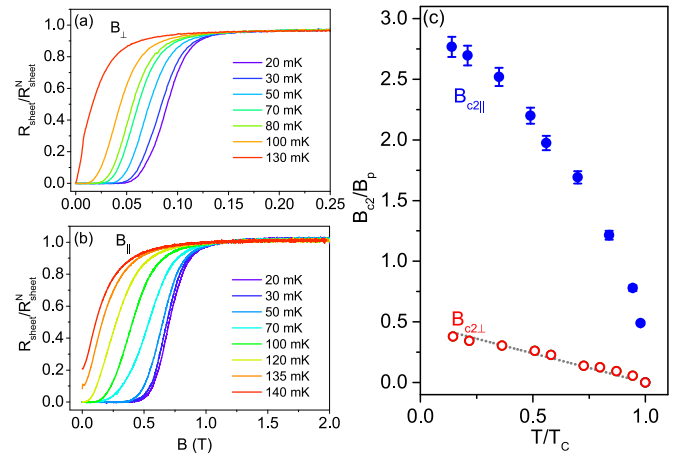

FIG. 1. Normalized sheet resistance versus temperature T as a function of (a) perpendicular field $B_\perp$ and (b) parallel magnetic field $B_\parallel$. (c) Upper critical field B_{c2} normalized by the Pauli paramagnetic field B_p as a function of reduced temperature T/T_C for fields applied parallel to the interface (blue filled circles) and perpendicular to the interface (red open circles). The gray dotted lines are fits to Eq. (1). The measurements were performed at $V_g = 200$ V.

sured to be about 140 mK. Figure 1(a) presents the normalized magnetoresistance $R_{\text{sheet}}/R_{\text{sheet}}^N$ as a function of perpendicular field $B_\perp$ at different temperatures for $V_g = 200$ V. Here, R_{sheet}^N is the zero-field normal-state sheet resistance measured at $T = 300$ mK. Fields of the order of 10 mT are enough to destroy the dissipationless superconducting state. The corresponding plots for $B_\parallel$ are shown in Fig. 1(b). As expected, given the quasi-2D nature of the system, the fields required in this case were at least two orders of magnitude higher.

In Fig. 1(c) we plot the upper-critical field B_{c2} [defined as the field at which the $R_{\text{sheet}}(B)$ drops to 40% of R_{sheet}^N] versus T for both $B_\perp$ and $B_\parallel$. The values of B_{c2} have been normalized by the BCS paramagnetic Pauli limit B_p, defined as $\sqrt{2}g\mu_B B_p = 3.5 k_B T_C$ [34,35]. g being the gyromagnetic ratio, k_B the Boltzmann constant, and μ_B the Bohr magneton. The dependence of B_{c2} on the temperature T for the out of plane is fitted well by the phenomenological 2D Ginzburg-Landau model [36]

$$B_{c2\perp} = \frac{\Phi_0}{2\pi \xi_{GL}(0)^2}(1 - T/T_c), \tag{1}$$

where $\xi_{GL}(0)$ is the in-plane GL coherence length at $T = 0$ K, $\Phi_0 = h/2e$ is the flux quantum. The value of $\xi_{GL}(0)$ extracted from the fit is 55 nm which matches well with previous reports [16,37]. From Fig. 1(c) we observe that $B_{c2\parallel}$ far exceeds the Clogston-Chandrasekhar limit which, in the weak coupling approximation, is expected to limit the value of the parallel upper critical field to $B_{c2\parallel} \leqslant B_p$. This large enhancement of $B_{c2\parallel}$ has been reported previously in (001) LaAlO$_3$/SrTiO$_3$ heterointerfaces [16] and has been postulated to arise from the presence of strong Rashba SOI which weakens spin paramagnetism by mixing the quasiparticle spin states [38,39]. Other possible mechanisms like anisotropic pairing mechanism, strong-coupling superconductivity, or other exotic many-body effects have been considered and ruled out by previous workers (see, for example, [16,40]).
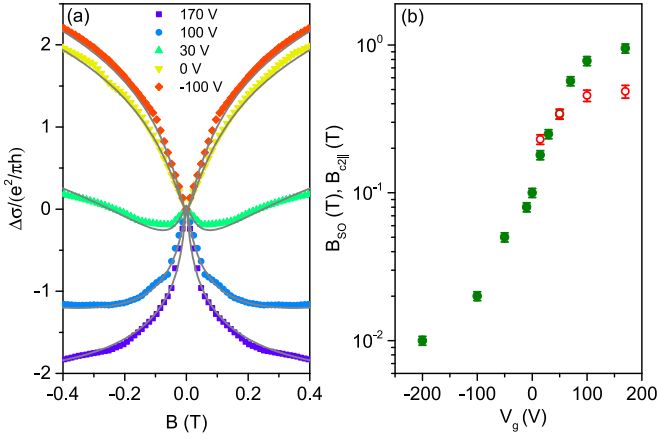
FIG. 2. (a) Magnetoconductance as a function of $B_\perp$ at different values of V_g. The scatter points are the measured data points while the solid lines are fits to Eq. (3). (b) Plot of B_{SO} (olive filled circles) and $B_{c2\parallel}$ (red filled circles) versus V_g. The measurements were performed at 245 mK.

For the case of strong SOI, $B_{c2\parallel}$ is related to the spin-orbit scattering time through [38]

$$\tau_{SO} = 0.362 \frac{\hbar}{k_B T_c} \left(\frac{B_P}{B_{c2\parallel}(0)} \right)^2. \quad (2)$$

Using this relation yields $\tau_{SO} = 4 \times 10^{-13}$ s for $V_g = 170$ V.

The SOI strength can also be extracted from the measured low-field magnetoconductance at $T > T_C$. In a two-dimensional system with in-plane SOI, in the presence of a perpendicular magnetic field $B_\perp$, the correction to conductance $\Delta\sigma$ takes the Maekawa-Fukuyama form [41]

$$\Delta\sigma(B) = \frac{e^2}{\pi h} \left[\Psi \left(\frac{B_\perp}{B_i + B_{SO}} \right) \right.$$

$$+ \frac{1}{2\sqrt{1-\gamma^2}} \Psi \left(\frac{B_\perp}{B_i + B_{SO}(1 + \sqrt{1-\gamma^2})} \right)$$

$$\left. - \frac{1}{2\sqrt{1-\gamma^2}} \Psi \left(\frac{B_\perp}{B_i + B_{SO}(1 - \sqrt{1-\gamma^2})} \right) \right]. \quad (3)$$

Here, $\Psi(x) = \ln(x) + \psi(0.5 + \frac{1}{x})$, where ψ is the digamma function. $B_i = \hbar/(4eD\tau_i)$ and $B_{SO} = \hbar/(4eD\tau_{SO})$ are inelastic and spin-orbit fields, respectively (τ_i and τ_{SO} are, respectively, the inelastic and spin-orbit scattering times), D is the diffusion constant, and γ is the Zeeman correction $\gamma = g\mu_B B/4eDB_{SO}$ (g and μ_B are the electron g factor and Bohr magnetron, respectively).

The low-field magnetoconductance at $T = 245$ mK is plotted in Fig. 2(a). From the fits to these curves we extract the τ_{SO} and B_{SO}. The value of τ_{SO} extracted from the fits to the magnetoresistance measured at $V_g = 170$ V is 1.6×10^{-13} s which matches closely with the value extracted using Eq. (2). The value of τ_{SO}, τ_i, and τ_{elas} (elastic scattering time) are shown in Fig. 11 in the Appendix. As shown in Fig. 2(b), the value of B_{SO} increases by almost two orders of magnitude as V_g is swept from -200 to 200 V. At low V_g, B_{SO} and $B_{c2\parallel}$ are comparable [Fig. 2(b)]. With increasing V_g, B_{SO} increases rapidly and becomes significantly larger than $B_{c2\parallel}$.
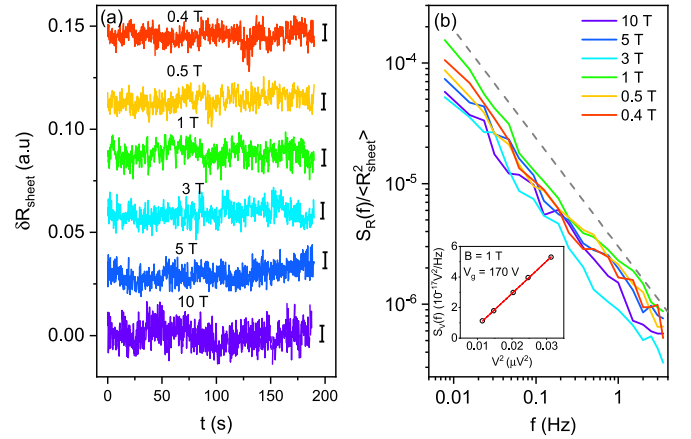

FIG. 3. (a) Time series of resistance fluctuations at a few representative values of $B_\parallel$. The measurement was performed at $T = 20$ mK and $V_g = 200$ V. (b) PSD of resistance fluctuations corresponding to the time series shown in (a). Inset: PSD is plotted as a function of V^2 at $B = 1$ T and $V_g = 170$ V; the linear dependence of $S_V(V)$ on V^2 establishes that noise originates from resistance fluctuations of the sample.

To probe the effect of spin-orbit interactions on charge carrier dynamics in the superconducting state, we studied resistance fluctuations for different magnetic fields at $T = 20$ mK ($T/T_C \approx 0.1$). The measurements were performed using a standard four-probe ac measurement technique (for details see Ref. [42]). Briefly, at each value of V_g and B, the device is biased by a small ac current and the time series of resistance fluctuations $\delta R_{sheet}(t)$ is measured for 30 min using a dual-phase digital lock-in amplifier. The output of the lock-in amplifier is recorded by a fast data acquisition (DAQ) card. After extensive digital filtering of $\delta R_{sheet}(t)$ to remove line frequency and aliasing effects, the power spectral density (PSD) of resistance fluctuations $S_R(f)$ was calculated using the method of Welch Periodogram. The time series of resistance fluctuations for a few representative values of $B_\parallel$, measured at $T = 20$ mK and $V_g = 200$ V, are plotted in Fig. 3(a). The corresponding PSD are shown in Fig. 3(b). For all values of V_g and B, the dependence of $S_R(f)$ on the frequency f was found to be of the form $S_R(f) \propto 1/f^\alpha$ with $\alpha \sim 0.9$–1. $S_V(f)$ was always found to depend quadratically on the voltage V developed across the channel [see inset of Fig. 3(b)] establishing that the measured noise originated from resistance fluctuations of the sample.

The PSD of resistance fluctuations was integrated over the measurement bandwidth (7 mHz–4 Hz) to obtain the relative variance of resistance fluctuations $\mathcal{R}$:

$$\mathcal{R} \equiv \frac{\langle \delta R_{sheet}^2 \rangle}{\langle R_{sheet}^2 \rangle} = \frac{1}{\langle R_{sheet}^2 \rangle} \int S_R(f) df. \quad (4)$$

In Fig. 4(a) we show the plots of relative variance of resistance fluctuations $\mathcal{R}$ as a function of $B_\parallel$ at a few representative values of V_g at $T = 20$ mK. At high $B_\parallel$, the noise has a very shallow dependence on the field. Below a certain characteristic field, which is specific to V_g, the noise increases rapidly with decreasing B. Normally, one would expect this characteristic field to be the upper critical field, above which
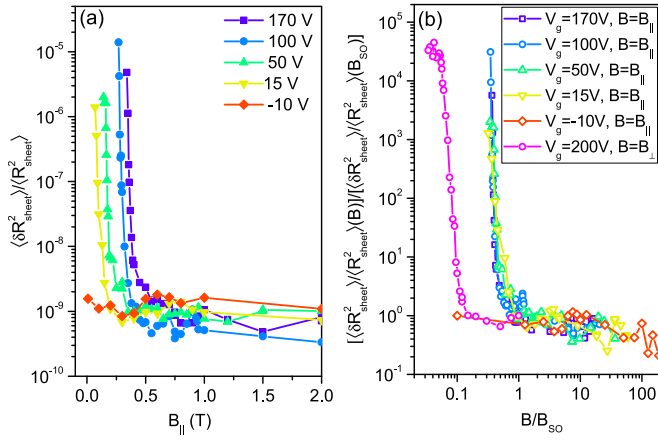
FIG. 4. (a) Plots of relative variance of resistance fluctuations $\mathcal{R}(B)$ versus $B_\parallel$, at different values of V_g. The measurements were performed at 20 mK. (b) Scaling plot of noise $\mathcal{R}(B)/\mathcal{R}(B_{SO})$ versus $B_\parallel/B_{SO}$ for V_g= 170, 100, 50, 15, and −10 V, respectively. Also plotted is $\mathcal{R}(B)/\mathcal{R}(B_{SO})$ versus $B_\perp/B_{SO}$ for field applied perpendicular to the interface at $V_g = 200$ V (magenta open circles).

superconducting fluctuations are suppressed. However, a closer inspection of the data reveals that the characteristic field scale in this case is the spin-orbit field B_{SO}. As the field decreases below B_{SO}, the noise increases rapidly, growing by over four orders of magnitude in the narrow magnetic field range $B_{c2\parallel} < B_\parallel < B_{SO}$. In Fig. 4(b) we show a scaling plot of the noise $\mathcal{R}(B)/\mathcal{R}(B_{SO})$ as a function of B/B_{SO}. The data for all $V_g > -10$ V collapse onto a single curve showing that indeed B_{SO} is the relevant scale governing the $B_\parallel$ dependence of the resistance fluctuations in a superconductor with strong SOI.

To understand the origin of the measured resistance fluctuations, we studied their higher-order statistics. Such studies have been used extensively to detect the presence of long-range correlations in systems undergoing magnetic, spin-glass, or superconducting transitions [22–28]. The central limit theorem states that for uncorrelated random fluctuators, the fluctuation statistics is Gaussian. As the correlation length in the system begins to diverge near a critical phase transition, the resultant time-dependent fluctuation statistics becomes strongly non-Gaussian [22–24,28]. We computed the "second spectrum" which is the four-point correlation function of the resistance fluctuations over a chosen frequency octave (f_l, f_h) [43,44]. It is mathematically defined as

$$S_R^{f_1}(f_2) = \int_0^\infty \langle \delta R^2(t) \rangle \langle \delta R^2(t+\tau) \rangle \cos(2\pi f_2 \tau) d\tau, \quad (5)$$

where f_1 is the center frequency of the chosen octave and f_2 the spectral frequency. Physically, $S_R^{f_1}(f_2)$ represents "spectral wandering" of the PSD with time. To avoid corruption of the signal by the Gaussian background noise, the second spectrum was calculated over the frequency octave 93.75–187.5 mHz, where the sample noise is significantly higher than the background noise. A convenient way of representing the second spectrum is through its normalized form $S_N^{(2)}$ defined as

$$S_N^{(2)} = \int_0^{f_h - f_l} S_R^{f_1}(f_2) df_2 \Big/ \left[\int_{f_l}^{f_h} S_R(f) df \right]^2. \quad (6)$$
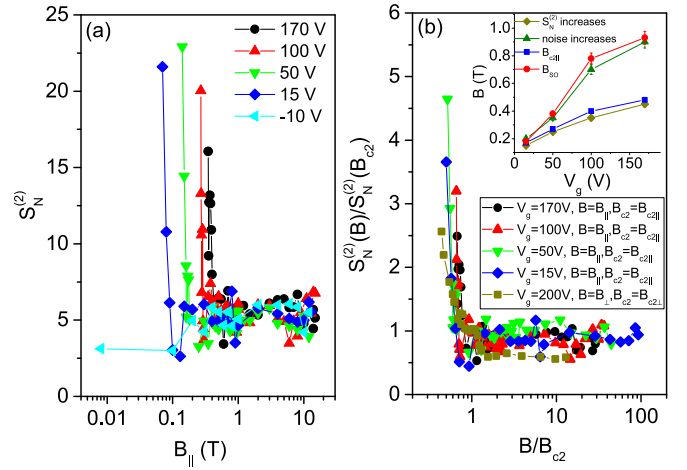

FIG. 5. (a) Plot of $S_N^{(2)}$ as a function of magnetic field applied parallel to the interface at different values of gate voltages. The measurement was performed at 20 mK. (b) Scaling plot of $S_N^{(2)}(B_\parallel)/S_N^{(2)}(B_{c2\parallel})$ versus $B_\parallel/B_{c2\parallel}$ for $V_g = 170$, 100, 50 and 15, V respectively. Also plotted is $S_N^{(2)}(B_\perp)/S_N^{(2)}(B_{c2\perp})$ versus $B_\perp/B_{c2\perp}$ for field applied perpendicular to the interface at $V_g = 200$ V (dark yellow squares).

For Gaussian fluctuations, $S_N^{(2)} = 3$. The measured values of $S_N^{(2)}$ as a function of $B_\parallel$ is shown in Fig. 5(a). We see that as the magnetic field is decreased below $B_{c2\parallel}$, $S_N^{(2)}$ starts increasing monotonically from its high-field value which was close to 3. This can be appreciated better from Fig. 5(b) where we plot $S_N^{(2)}(B_\parallel)/S_N^{(2)}(B_{c2\parallel})$ as a function of $B_\parallel/B_{c2\parallel}$. The data for all V_g collapse onto a single plot showing that the relevant field scale for the second spectrum is $B_{c2\parallel}$. We note that scaling plot $S_N^{(2)}(B_\parallel)/S_N^{(2)}(B_{c2\parallel})$ remains unchanged if $B_{c2\parallel}$ are defined for other resistance criterion, e.g., $R_{sheet} = 0.7R_{sheet}^N$ and $R_{sheet} = 0.1R_{sheet}^N$ (see Fig. 6). For $V_g = -10$ V, where the device is in resistive state over the entire magnetic field range, the relative variance of resistance fluctuations $\mathcal{R}$ is independent of field (Fig. 4) and $S_N^{(2)} \simeq 3$ (Fig. 5) showing that the fluctuations in the normal state in LaAlO$_3$/SrTiO$_3$ are Gaussian.
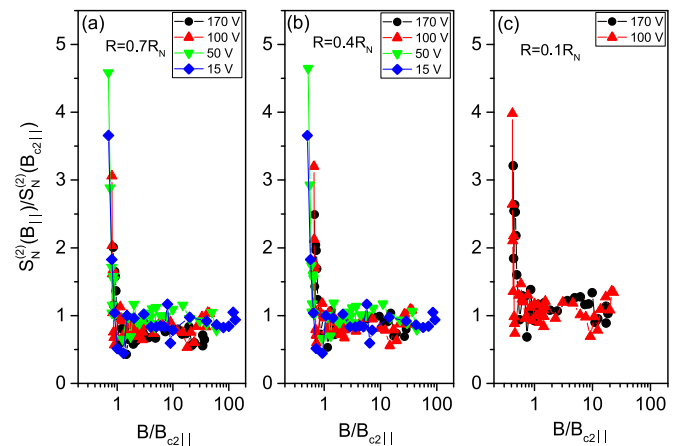

FIG. 6. Scaling plot of $S_N^{(2)}(B)/S_N^{(2)}(B_{c2\parallel})$ versus $B_\parallel/B_{c2\parallel}$. B_{c2} are defined from the resistance transition at (a) $0.7R_{sheet}^N$, (b) $0.4R_{sheet}^N$, and (c) $0.1R_{sheet}^N$ resistance criterion.

To summarize our observations so far: (a) for $B_\parallel > B_{SO}$, the resistance fluctuations are almost independent of $B_\parallel$ and have a Gaussian distribution, (b) there is a significant range of field $B_{SO} > B_\parallel > B_{c2\parallel}$ where the resistance fluctuations depend strongly on $B_\parallel$ while remaining Gaussian, and (c) for $B_\parallel < B_{c2\parallel}$, the resistance fluctuations are large, have a strong $B_\parallel$ dependence, and have a non-Gaussian distribution. In the inset of Fig. 5(b) we summarize the data. One can see that the magnetic field at which the second spectrum deviates from the Gaussian value (we call it B_{NG}) closely follows the upper critical field $B_{c2\parallel}$ while the field at which the noise begins to shoot up (labeled B_N) tracks B_{SO}. At this point it is profitable to compare these observations with what is seen for $B_\perp$ for this q-2DEG superconductor, representative data taken at $T = 20$ mK and $V_g = 200$ V is plotted in Fig. 4(b) (magenta open circles). For $B_\perp > B_{c2\perp}$, the noise is field independent, small in magnitude and Gaussian. For $B_\perp < B_{c2\perp}$, the noise is non-Gaussian and diverges strongly as the field is reduced [Fig. 5(b), dark yellow squares]. Notably, in contrast to $B_\parallel$, the divergence of noise and appearance of non-Gaussian component are concurrent. This has been observed previously in other two-dimensional superconductors and has been shown to arise due to long-range correlations between the vortices near the transition [24,27,45–48].

We now discuss the possible origin of the decoupling of B_{NG} and B_N in this system. As shown before [24,27], it is correlations between vortices that leads to non-Gaussian noise in 2D superconductors. Thus, it is natural that $B_{c2\parallel}$ (the field at which superconductivity is destroyed) and B_{NG} (the field at which non-Gaussian fluctuations vanish) coincide. The measured resistance fluctuations, however, persist beyond $B_{c2\parallel}$ deep into the normal state, until $B_\parallel \sim B_{SO}$. Below we present a plausible scenario which explains this. Strong SOI present in this system ensures that the electronic spins are all in plane. As the electronic transport is diffusive, the k vector of the charge carriers take random values. Spin-momentum locking due to SOI causes these charge carriers to feel an effective in-plane B_{SO} field perpendicular to the k vector. The competition of this random B_{SO} with $B_\parallel$ brings down the in-plane spin magnetic moment to $\sim (B_\parallel/B_{SO})\mu_B$ [4,49,50]. At large enough parallel magnetic fields, Zeeman energy ensures that all the spins are aligned along $B_\parallel$. As $B_\parallel$ is reduced to the order of B_{SO} there begin to appear spins of opposite signs which can form Cooper pairs. With further reduction of $B_\parallel$, the superfluid density grows and for $B_\parallel < B_{c2\parallel}$ global phase coherence sets in. Thus, in the field range $B_{SO} > B_\parallel > B_{c2\parallel}$ there will exist domains of superconducting clusters in a background of normal carriers. We propose that it is fluctuations of these superconducting clusters that give rise to the large Gaussian noise over this field regime. We present a schematic phase diagram of the spin orientation in Fig. 7 in the SOI energy ε_{SOI} and $B_\parallel$ plane. The values of ε_{SOI} have been obtained from τ_{SO} extracted from the fits to the magnetoresistance data at different V_g using Eq. (3). This picture is in some sense analogous to what one gets in the zero-field limit; as the temperature is reduced sufficiently close to T_C, there appear percolating clusters with finite superfluid density in a resistive background which gives rise to large Gaussian resistance fluctuations. It has been predicted that FFLO state is favorable in the phases between B_{c2} and B_{SO} [51,52], which
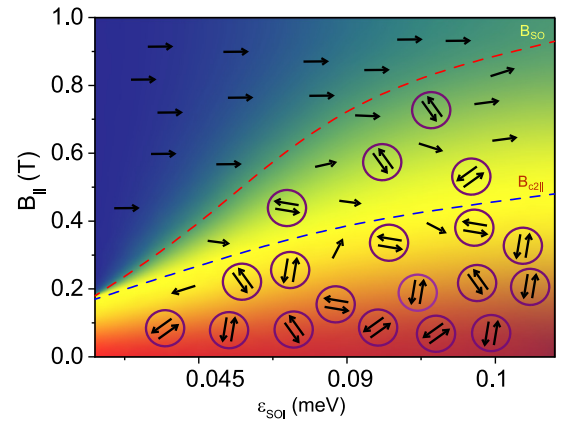

FIG. 7. Schematic phase diagram showing the spin orientations at the LaAlO$_3$/SrTiO$_3$ interface. Upper critical field $B_{c2\parallel}$ (blue line) and spin-orbit field B_{SO} (red line) have been plotted in the SOI-energy ϵ_{SOI} and $B_\parallel$ plane. Arrows indicate the direction of spin of a single electron in the plane of the q-2DEG while circles represent the Cooper pairs.

possibly can have contributions to the resistance fluctuations. Without experimental data, we refrain commenting on it.

The magnetic-field-induced transition to the superconducting state is affected by nonmagnetic disorder [53,54] and the transition is assumed to be percolative in nature. To describe such a percolative phase transition induced by in-plane magnetic field B, a random resistor network (RRN) model was considered [55,56]. In this model, we consider a square network of identical resistors of size $L \times L$, where L is the number of grid points along x or y direction. In the ideal scenario, the resistor network is assumed to be connected by external conducting wires to a voltage source V, which causes a current I to flow through the network, so that the macroscopic sheet resistance is measured as $R_{sheet} = V/I$. In this model, we discretize the resistance and define the mean resistance at a grid point (x_i, y_i) by R_i, so that the macroscopic resistance is given by averaging over all grid points in the network, viz., $R_{sheet} = (1/L^2)\sum_i R_i$.

In the RRN model, we consider a 100×100 network in which circular resistive clusters appear in the superconducting phase when B is increased, as shown in Fig. 8. The B dependence of the number and diameter of the clusters are given, respectively, by $N_{cluster} = \text{Int}(C_1(B - B_c))$ and $D_{cluster} = C_2 B_r$, where $B_r = (B - B_c)/B_c$, B_c is the critical field for the superconducting transition (at a given value of gate voltage V_g, we take B_c as the highest available critical field, i.e., $B_c = B_{SO}$), C_1 and C_2 are parameters which are determined by fitting R with experimental data, the function $\text{Int}(\dots)$ returns the integer value of the number inside the bracket. The value of the resistance inside the resistive clusters is large, here we assume $R_{sheet} = R_{sheet}^N$, the value in the normal metallic state at $B = 2$ T. The normalized resistance at a field B is given by $R/R_N = 1/(1 + \xi^2)$, where ξ is the superconducting coherence length. We assume that in a disordered BCS superconductor with percolative superconducting transition, ξ follows a field dependence which is similar to the temperature dependence, predicted by Halperin-Nelson equation, and can be expressed as $\xi = (2/A)\sinh(b/\sqrt{B_r})$,
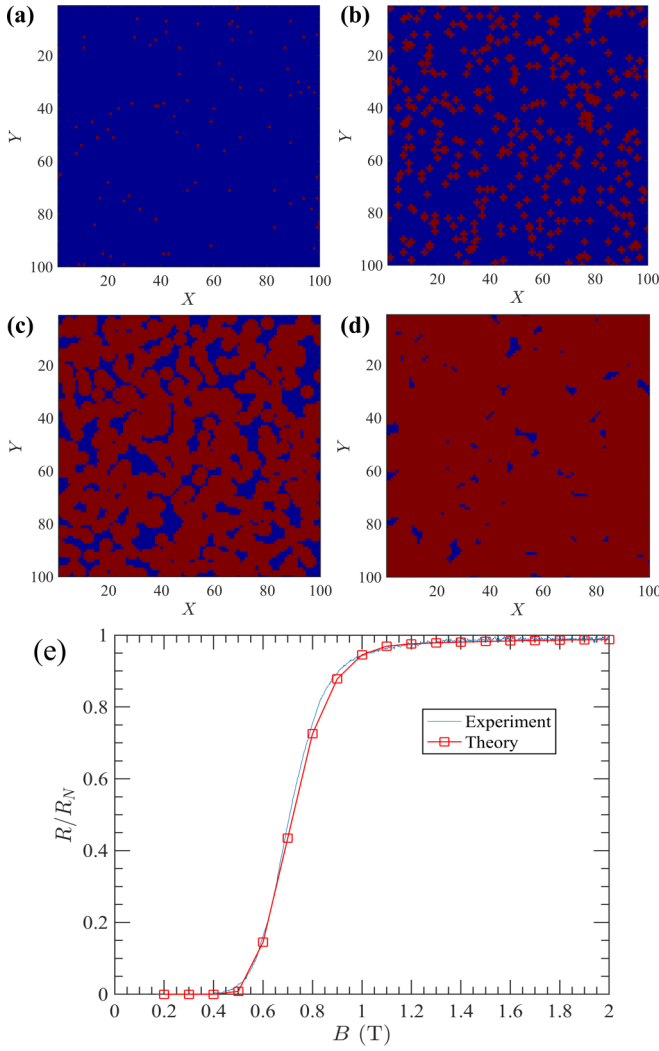
FIG. 8. Color map of the sheet resistance R_{sheet} in a 100×100 network in the RRN model at different in-plane magnetic fields (a) $B_\parallel = 1$ T, (b) $B_\parallel = 1.3$ T, (c) $B_\parallel = 1.6$ T, and (d) $B_\parallel = 1.9$ T, across the transition from superconducting state to the normal metallic state. Blue background denotes regions with resistance $R_{\text{sheet}} = 0$, while red dots/patches denote regions with high resistance $R_{\text{sheet}} = R^N_{\text{sheet}}$ ($R_{\text{sheet}} = R^N_{\text{sheet}}$ being the resistance in the normal metallic state). In this plot, temperature $T = 20$ mK and gate voltage $V_g = 170$ V. (e) The blue line shows the variation of the normalized resistance $R_{\text{sheet}}/R^N_{\text{sheet}}$ (blue curve) with in-plane magnetic field $B_\parallel$ at $T = 20$ mK and $V_g = 170$ V, where R^N_{sheet} is the resistance in the normal metallic state. The theoretical fit obtained using the RRN model is shown by the red open circles.

where A and b are parameters which are determined by fitting with experimental data. By fitting the experimental data at $T = 20$ mK and $V_g = 170$ V, we obtain $A = 1.8$, $b = 0.2$, $C_1 = 1000$, and $C_2 = 1.65$. The data have been plotted in Fig. 8(e). Spatial inhomogeneity on the two-dimensional superconductor broadens the BKT transition [27,57] and a percolation transition is well accessible within the Halperin-Nelson theory.

The resistance at position (x_i, y_i) at a magnetic field B and time t is given by $R_i(B, t) = R_i(B) + \delta R_i(B, t)$. We start at $B = 0.2$ T with $\delta R_i(B, t = 0) = 0$ and continuously update
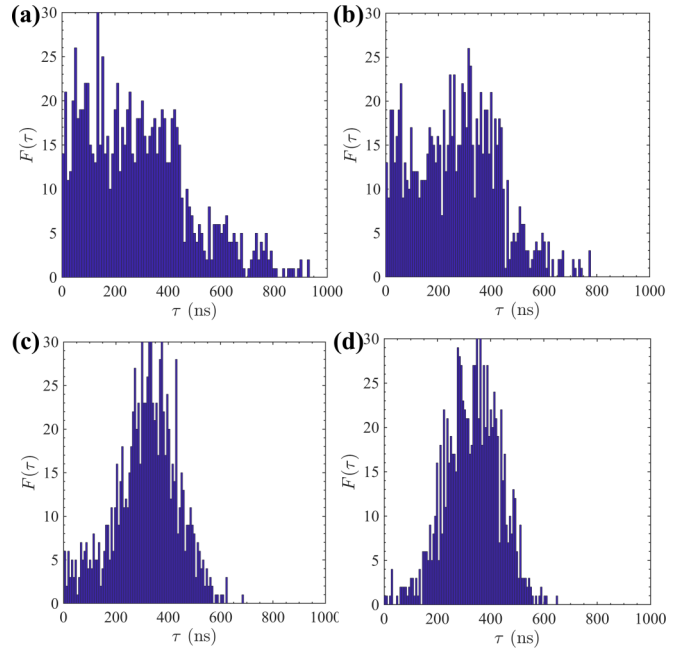

FIG. 9. Distribution of the relaxation time at different in-plane magnetic field $B_\parallel$ values (a) 1 T, (b) 1.3 T, (c) 1.6 T, and (d) 1.9 T. The distribution changes from non-Gaussian type to Gaussian type as $B_\parallel$ is increased across the transition from superconducting state to normal-metallic state. In this plot, $T = 20$ mK and $V_g = 170$ V.

$R_i(B, t)$ at the interval of a relaxation time τ and finally reach the maximum field $B = 2$ T. The amplitude of noise $\delta R_i(B, t)$ is chosen randomly from a set $\{\delta R_i(B, t)\}$ of numbers which follows Gaussian distribution and has a standard deviation 0.001 and zero mean. The statistics of the noise is, however, governed by the distribution of τ which is also chosen randomly from a set $\{\tau_n\}$. We assume that the Josephson junctions, formed during the percolative superconducting transition, contribute non-Gaussian component in the resistance noise. We, therefore, consider that the distribution of the relaxation time has two components which can be expressed as $\{\tau_n\} = x\{\tau_n\}_{\text{NGC}} + (1 - x)\{\tau_n\}_{\text{GC}}$, NGC stands for non-Gaussian component and GC for Gaussian component. The fraction x, which defines the amount of non-Gaussianity in the noise, is taken to be proportional to the ratio of the superconducting region to the nonsuperconducting region. The distribution functions for $\{\tau_n\}_{\text{NGC}}$ and $\{\tau_n\}_{\text{GC}}$ are determined by comparing the frequency dependence of power spectral density (PSD) of resistance noise, given by the following equation, with the experimentally obtained PSD:

$$S_R(f) = \lim_{t_0 \to \infty} \left(\frac{1}{2t_0} \right) \left(\int_{-t_0}^{t_0} \delta R(t) e^{i2\pi ft} dt \right)^2. \quad (7)$$

To incorporate the $1/f$ dependence of PSD and the influence of SOI, we include the second critical field $B_{c2\parallel}$ in the PSD, through the following relation:

$$S_R(f) = \int_0^\infty d\tau\, F(\tau) \frac{2\tau(B - B_{c2\parallel})^3}{1 + 2\pi f\tau}, \quad (8)$$

where $F(\tau)$ is the distribution function for τ. For the GC, we have a Gaussian distribution $F(\tau) = 1/(\sqrt{2\pi\sigma^2}) e^{-(\tau - \tau_{\text{GC}})^2/2\sigma^2}$, where σ and τ_{GC} are, respectively,
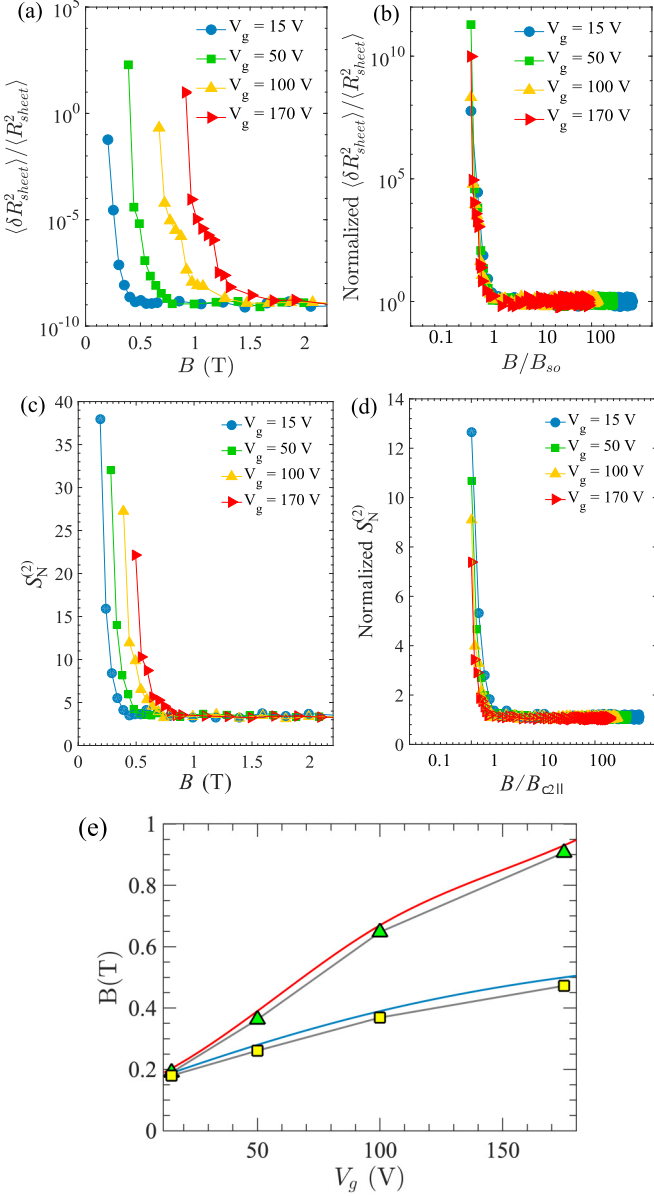
FIG. 10. Gate-voltage variation of (a) $\mathcal{R}$ with magnetic field B, (b) normalized $\mathcal{R}$ with B/B_{so}, (c) $S_N^{(2)}$ with magnetic field B and (d) normalized $S_N^{(2)}$ with $B/B_{c2||}$ at different values of gate-voltage V_g. The normalization of the quantities, plotted on the vertical axis, in (b) and (d) is performed using the respective values at the maximum value of the B field. In this plot, temperature $T = 20$ mK. (e) Variation of the critical fields $B_{c2||}$ (yellow squres) and B_{so} (blue traingles) with gate-voltage. The modeled gate-voltage dependence is obtained from Fig. 7.

as a function of the field B for different representative values of gate voltage V_g are shown in Figs. 10(a) and 10(c). The same set of obtained data, when plotted with respect to the field values, scaled using the critical fields B_{SO} and $B_{c2||}$, reveals that $\mathcal{R}$ scales with B_{SO} while $S_N^{(2)}$ scales with $B_{c2||}$, as shown in Figs. 10(b) and 10(d). The critical fields $B_{c2||}$ (yellow squres) and spin-orbit fields B_{SO} (blue traingles), obtained from the simulation are shown as a function of V_g along with experiment in Fig. 10(e). The excellent match between experimental and simulation data tells that a simple random resistor network model is able to capture the essential features of resistance fluctuations close to the upper critical field in 2D inversion-symmetry-broken superconductors.

IV. CONCLUSION

To conclude, we have probed, through careful measurements of resistance fluctuations, the interplay of SOI, pairing potential and Zeeman energy in the superconducting phase of $LaAlO_3/SrTiO_3$. We find the presence of larger non-Gaussian fluctuations below $B_{c2||}$ arising due to correlated vortex dynamics. Large, Gaussian resistance fluctuations were seen in the field range between $B_{c2||}$ and B_{SO} which indicate the presence of superconducting clusters without global phase coherence. We identify and quantify the relevant energy scales in this system: SOI, Zeeman energy, and pairing potential. Our work emphasizes the important role played by the interplay between these energy scales in framing the phase diagram of 2D inversion asymmetric superconductors.

APPENDIX

In Fig. 11, we plot the different scattering times extracted from Eq. (3) as a function of V_g at $T = 245$ mK. It can be seen

the variance and mean value of the Gaussian distribution. For the NGC, we use a stretched exponential function $F(\tau) = 1/(2\sqrt{\pi})\sqrt{\tau}e^{-\tau/\tau_{NGC}}$, typically used to study glassy dynamics. With $\tau_{GC} = \tau_{NGC} = 500$ ns and $\sigma = 100$ ns, the PSDs are calculated at different fields and the corresponding distributions of $\{\tau_n\}$ are shown in Fig. 9.

The relative variance of the resistance fluctuations $\mathcal{R} \equiv \frac{\langle \delta R_{sheet}^2 \rangle}{\langle R_{sheet}^2 \rangle}$ and the normalized second spectrum $S_N^{(2)}$ are calculated by using Eqs. (4) and (6), respectively. A plot of $\mathcal{R}$ and $S_N^{(2)}$
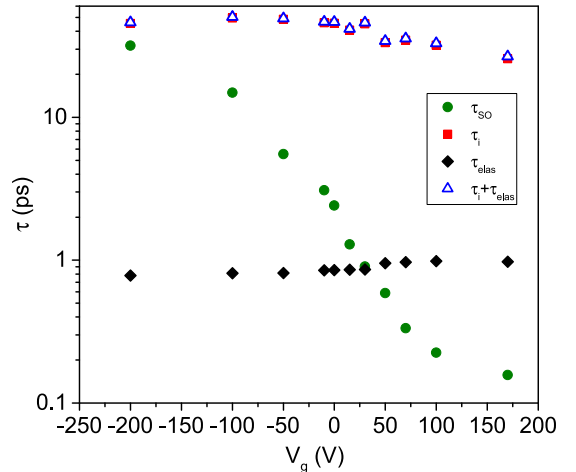

FIG. 11. Plot of spin-orbit scattering time τ_{SO} (olive filled circles), inelastic time τ_i (red filled squares), elastic time τ_{elas} (black filled), and total scattering time $\tau = \tau_i + \tau_{elas}$ (blue open triangles) versus V_g.

that for all V_g, total scattering time τ ($=\tau_i + \tau_{elas}$, where τ_i and τ_{elas} are inelastic and elastic scattering time, respectively) is larger than spin-orbit scattering time τ_{SO}, implying strong spin-orbit interaction in the LaAlO$_3$/SrTiO$_3$ interface which is gate voltage tunable.

[1] M. Sigrist and K. Ueda, Rev. Mod. Phys. **63**, 239 (1991).

[2] P. Fulde and R. A. Ferrell, Phys. Rev. **135**, A550 (1964).

[3] P. W. Anderson, Phys. Rev. B **30**, 4000 (1984).

[4] M. Sigrist, in *Lectures on the Physics of Strongly Correlated Systems XIII: Thirteenth Training Course in the Physics of Strongly Correlated Systems*, edited by A. Avella and F. Mancini, AIP Conf. Proc. No. 1162 (AIP, Melville, NY, 2009), pp. 55–96.

[5] H. Fukazawa and K. Yamada, J. Phys. Soc. Jpn. **72**, 2449 (2003).

[6] C. Petrovic, P. Pagliuso, M. Hundley, R. Movshovich, J. Sarrao, J. Thompson, Z. Fisk, and P. Monthoux, J. Phys.: Condens. Matter **13**, L337 (2001).

[7] A. Huxley, I. Sheikin, E. Ressouche, N. Kernavanois, D. Braithwaite, R. Calemczuk, and J. Flouquet, Phys. Rev. B **63**, 144519 (2001).

[8] Y. Yin, M. Zech, T. L. Williams, X. F. Wang, G. Wu, X. H. Chen, and J. E. Hoffman, Phys. Rev. Lett. **102**, 097002 (2009).

[9] K. V. Samokhin, E. S. Zijlstra, and S. K. Bose, Phys. Rev. B **69**, 094514 (2004).

[10] Y. Tada, N. Kawakami, and S. Fujimoto, Phys. Rev. B **81**, 104506 (2010).

[11] N. Kimura, K. Ito, H. Aoki, S. Uji, and T. Terashima, Phys. Rev. Lett. **98**, 197001 (2007).

[12] L. P. Gor'kov and E. I. Rashba, Phys. Rev. Lett. **87**, 037004 (2001).

[13] K. Michaeli, A. C. Potter, and P. A. Lee, Phys. Rev. Lett. **108**, 117003 (2012).

[14] S. Caprara, F. Peronaci, and M. Grilli, Phys. Rev. Lett. **109**, 196401 (2012).

[15] Z. Zhong, A. Tóth, and K. Held, Phys. Rev. B **87**, 161102(R) (2013).

[16] M. Ben Shalom, M. Sachs, D. Rakhmilevitch, A. Palevski, and Y. Dagan, Phys. Rev. Lett. **104**, 126802 (2010).

[17] A. D. Caviglia, M. Gabay, S. Gariglio, N. Reyren, C. Cancellieri, and J.-M. Triscone, Phys. Rev. Lett. **104**, 126803 (2010).

[18] A. Caviglia, S. Gariglio, N. Reyren, D. Jaccard, T. Schneider, M. Gabay, S. Thiel, G. Hammerl, J. Mannhart, and J.-M. Triscone, Nature (London) **456**, 624 (2008).

[19] N. Mohanta and A. Taraphder, Phys. Rev. B **92**, 174531 (2015).

[20] M. Smidman, M. B. Salamon, H. Q. Yuan, and D. F. Agterberg, Rep. Prog. Phys. **80**, 036501 (2017).

[21] N. Mohanta and A. Taraphder, Europhys. Lett. **108**, 60001 (2014).

[22] M. Weissman, Rev. Mod. Phys. **65**, 829 (1993).

[23] S. Joubaud, A. Petrosyan, S. Ciliberto, and N. B. Garnier, Phys. Rev. Lett. **100**, 180601 (2008).

[24] R. Koushik, S. Kumar, K. R. Amin, M. Mondal, J. Jesudasan, A. Bid, P. Raychaudhuri, and A. Ghosh, Phys. Rev. Lett. **111**, 197001 (2013).

[25] S. Samanta, A. K. Raychaudhuri, and Y. M. Mukhovskii, Phys. Rev. B **85**, 045127 (2012).

[26] G. N. Daptary, C. Sow, P. S. Anil Kumar, and A. Bid, Phys. Rev. B **90**, 115153 (2014).

[27] G. N. Daptary, S. Kumar, P. Kumar, A. Dogra, N. Mohanta, A. Taraphder, and A. Bid, Phys. Rev. B **94**, 085104 (2016).

[28] G. N. Daptary, P. Kumar, A. Dogra, and A. Bid, Phys. Rev. B **98**, 035433 (2018).

[29] M. Kawasaki, K. Takahashi, T. Maeda, R. Tsuchiya, M. Shinohara, O. Ishiyama, T. Yonezawa, M. Yoshimoto, and H. Koinuma, Science **266**, 1540 (1994).

[30] P. Kumar, A. Dogra, P. Bhadauria, A. Gupta, K. Maurya, and R. Budhani, J. Phys.: Condens. Matter **27**, 125007 (2015).

[31] A. Joshua, S. Pecker, J. Ruhman, E. Altman, and S. Ilani, Nat. Commun. **3**, 1129 (2012).

[32] Y.-L. Han, S.-C. Shen, J. You, H.-O. Li, Z.-Z. Luo, C.-J. Li, G.-L. Qu, C.-M. Xiong, R.-F. Dou, L. He *et al.*, Appl. Phys. Lett. **105**, 192603 (2014).

[33] G. N. Daptary, S. Kumar, A. Bid, P. Kumar, A. Dogra, R. C. Budhani, D. Kumar, N. Mohanta, and A. Taraphder, Phys. Rev. B **95**, 174502 (2017).

[34] B. Chandrasekhar, Appl. Phys. Lett. **1**, 7 (1962).

[35] A. M. Clogston, Phys. Rev. Lett. **9**, 266 (1962).

[36] M. Tinkham, Phys. Rev. **129**, 2413 (1963).

[37] N. Reyren, S. Gariglio, A. Caviglia, D. Jaccard, T. Schneider, and J.-M. Triscone, Appl. Phys. Lett. **94**, 112506 (2009).

[38] R. A. Klemm, A. Luther, and M. R. Beasley, Phys. Rev. B **12**, 877 (1975).

[39] P. M. Tedrow and R. Meservey, Phys. Rev. B **25**, 171 (1982).

[40] P. K. Rout, E. Maniv, and Y. Dagan, Phys. Rev. Lett. **119**, 237002 (2017).

[41] S. Maekawa and H. Fukuyama, J. Phys. Soc. Jpn. **50**, 2516 (1981).

[42] A. Ghosh, S. Kar, A. Bid, and A. Raychaudhuri, arXiv:cond-mat/0402130.

[43] P. J. Restle, R. J. Hamilton, M. B. Weissman, and M. S. Love, Phys. Rev. B **31**, 2254 (1985).

[44] G. T. Seidler and S. A. Solin, Phys. Rev. B **53**, 9753 (1996).

[45] T. J. Shaw, M. J. Ferrari, L. L. Sohn, D.-H. Lee, M. Tinkham, and J. Clarke, Phys. Rev. Lett. **76**, 2551 (1996).

[46] P. H. E. Tiesinga, T. J. Hagenaars, J. E. van Himbergen, and J. V. José, Phys. Rev. Lett. **78**, 519 (1997).

[47] I.-J. Hwang and D. Stroud, Phys. Rev. B **57**, 6036 (1998).

[48] K. H. Wagenblast and R. Fazio, J. Exp. Theor. Phys. Lett. **68**, 312 (1998).

[49] X. Xi, Z. Wang, W. Zhao, J.-H. Park, K. T. Law, H. Berger, L. Forró, J. Shan, and K. F. Mak, Nat. Phys. **12**, 139 (2016).

[50] S. J. Youn, M. H. Fischer, S. H. Rhim, M. Sigrist, and D. F. Agterberg, Phys. Rev. B **85**, 220505(R) (2012).

[51] V. Barzykin and L. P. Gor'kov, Phys. Rev. Lett. **89**, 227002 (2002).

[52] O. Dimitrova and M. V. Feigel'man, Phys. Rev. B **76**, 014522 (2007).

[53] N. Mohanta and A. Taraphder, J. Phys.: Condens. Matter **26**, 215703 (2014).

[54] N. Mohanta and A. Taraphder, J. Phys.: Condens. Matter **26**, 025705 (2013).

[55] R. Rammal, C. Tannous, P. Breton, and A. M. S. Tremblay, Phys. Rev. Lett. **54**, 1718 (1985).

[56] C. C. Chen and Y. C. Chou, Phys. Rev. Lett. **54**, 2529 (1985).

[57] L. Benfatto, C. Castellani, and T. Giamarchi, Phys. Rev. B **80**, 214506 (2009).